Vol.43 No.1　2019

Journal

JOURNAL OF THE MAGNETICS SOCIETY OF JAPAN

*Vol.*43 *No.*1 **2019**
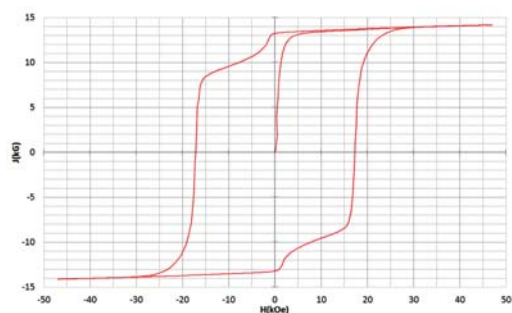
世界初！高温超電導型VSM

新製品

世界初*、高温超電導マグネットをVSMに採用することで測定速度 当社従来機1/20を実現。
0.5mm cube磁石のBr, HcJ高精度測定が可能となりました。
*2014年7月 東英工業調べ

測定結果例

高温超電導VSMによるNdFeB（sint.）0.5mm cube BHカーブ

磁化測定レンジ：0.2emu
Br = 13.2kG   HcJ = 17.2kOe

高温超電導VSMによるNdFeB（sint.）1mm cube BHカーブ
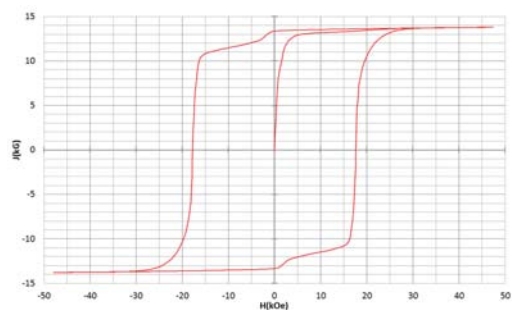
磁化測定レンジ：2emu
Br = 13.3kG   HcJ = 17.7kOe

高温超電導VSMによるNdFeB（sint.）4mm cube BHカーブ
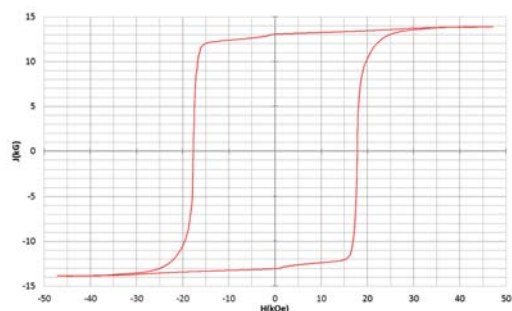
磁化測定レンジ：100emu
Br = 13.1kG   HcJ = 17.8kOe

高速測定を実現

高温超電導マグネット採用により、高速測定を実現しました。Hmax＝5Tesla, Full Loop測定が2分で可能です。
（当社従来機：Full Loop測定 40分）

小試料のBr,HcJ高精度測定

0.5mm cube磁石のBr,HcJ高精度測定ができ、表面改質領域を切り出しBr,HcJの強度分布等、微小変化量の比較測定が可能です。
また、試料の加工劣化の比較測定が可能です。

試料温度可変測定

－50℃～＋200℃温度可変UNIT（オプション）

磁界発生部の小型化

マグネットシステム部寸法：0.8m×0.3m×0.3m

COMSOL MULTIPHYSICS®

有限要素法解析ソフトウェア COMSOL Multiphysics®

マルチフィジックスの進化論

無制限・強連成で実現象に即したシミュレーション事例のご紹介

永久磁石を利用した磁気軸受の解析例

体積: Magnetic flux density norm (T)

グローバル: Sensitivity of Fz w.r.t. dZ [N/m]

面: Magnetic flux density norm (T) コンタ: Magnetic vector potential, phi component (Wb/m)
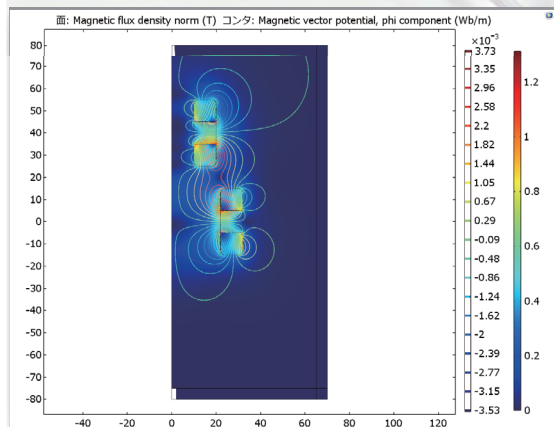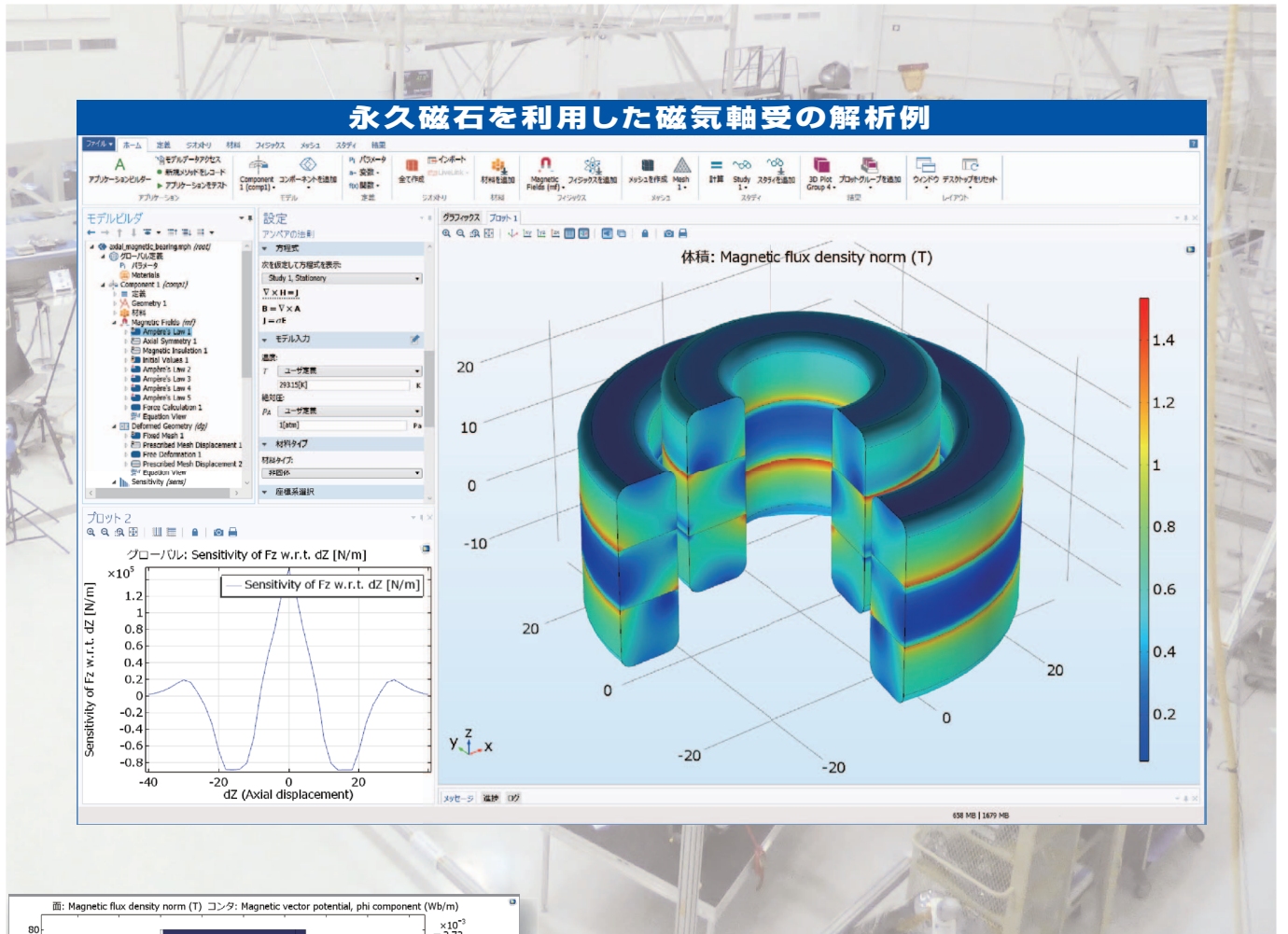
AC/DC モジュールの適用例

- ・AC/DC 電流分布、電場分布
- ・バイオヒーティング
- ・コイルとソレノイド
- ・SPICE 回路とフィールドシミュレーション
- ・接触抵抗
- ・電磁両立性 (EMC) および電磁妨害 (EMI)
- ・電磁力およびトルク
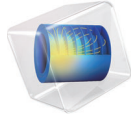- ・電磁力シールド
- ・電気機械の変形
- ・ホール効果を利用したセンサ

- ・インシュレータ、コンデンサ、誘電体
- ・モータ、ジェネレータ、および他の電気機械
- ・非線形材料
- ・寄生容量とインダクタンス
- ・永久磁石と電磁石
- ・多孔質材料
- ・抵抗および誘導加熱
- ・センサ
- ・超伝導体
- ・変圧器とインダクタ

永久磁石を使用した磁気軸受

永久磁石を使用した軸受はターボ機械、ポンプ、モータ、発電機やフライホイール式エネルギー貯蔵システムなど、様々な分野で使用されています。非接触かつ潤滑不要で保守整備を大幅に省略できる点は、従来の機械式ベアリングと比べて重要なメリットです。この例では、軸方向の永久磁石軸受の磁気力や剛性などの設計パラメータを計算する方法を示しています。

※AC/DCモジュールはCOMSOL Multiphysicsと併用するアドオン製品です。

COMSOL Multiphysics® なら、今まで不可能だった 3 種以上のマルチフィジックス解析を強連成で実現できます。30 日間全機能無料トライアル、無料の導入セミナー、1000 種を超える世界の様々な事例をご提供いたします。詳しくは、下記の弊社営業部までお問い合せください。

COMSOL
http://www.comsol.jp

KESCO KEISOKU ENGINEERING SYSTEM
計測エンジニアリングシステム株式会社
http://www.kesco.co.jp/comsol/
Tel：03-5282-7040 ・ Fax：03-5282-0808

Journal of the Magnetics Society of Japan
Vol. 43, No. 1

CONTENTS

Board of Directors of The Magnetics Society of Japan

<Paper>

Magnetoresistance in bilayers of heavy metal and non-collinear antiferromagnet

K. Oda, T. Moriyama[a], and T. Ono

Institute for Chemical Research, Kyoto University, Uji, Kyoto, 611-0011, Japan

We report on magnetoresistance measurements in a heavy metal/ Mn_3Ir multilayers. After a post annealing process, we observed the magnetoresistance associated with the ordered crystalline structure of the Mn_3Ir. The resistance change as a function of the strength as well as the direction of the applied field suggests that the magnetoresistance is partially related to a modification of the Néel order by the magnetic field. Our further detailed investigation revealed that there is an additional component of the resistance change, perhaps due to the non-collinear magnetic structure associated with the $L1_2$-ordered Mn_3Ir, which cannot be accounted for by any conventional magnetoresistance effects.

a)   mtaka@scl.kyoto-u.ac.jp

1. Introduction

Antiferromagnetic spintronics is an emerging field which utilizes antiferromagnets (AFMs) as active components in spintronic applications [1),2)]. Compared to ferromagnets (FMs), AFMs have several appealing properties, e. g., zero stray field, robustness against magnetic field perturbations, and ultrafast dynamics, leading to an ultrahigh density memory and ultrafast information processing. However, in other words, the insensitivity to an external magnetic field makes electrical manipulation and detection of the Néel order in AFMs quite challenging. Especially, the difficulty of the electrical detection obstructs experimental advances of antiferromagnetic spintronics as opposed to the ferromagnetic spintronics.

Nevertheless, recent studies have demonstrated the electrical detection of the Néel order in some of the antiferromagnetic materials by the same principle having been used for ferromagnetic materials: i.e. anisotropic magnetoresistance (AMR) [3)] and the spin Hall magnetoresistance (SMR) [4),5)]. AMR and SMR depend on the square of the spontaneous magnetization, these magnetoresistances in principle appear not only in FMs but also in the AFMs [6)]. These magnetoresistances have been reported in some of the particular collinear AFMs, such as FeRh [7),8)], NiO [9)-12)], CuMnAs [13)], and Mn_2Au [14)-16)], etc. in which the Néel order control is evidently possible.

More intriguing magnetoresistive effect in AFMs is the giant anomalous Hall effect (AHE) not due to the magnetic moments themselves but due to the chiral magnetic structure [17)]. Chen *et al.* theoretically predicted that such an AHE can be observed in $L1_2$ ordered Mn_3Ir in which the magnetic moments make a triangle lattice. Later, the giant anomalous Hall effect (AHE) was experimentally reported for a similar material system, i.e. Mn_3Sn [18)].

As the electrical detection of the magnetic state in AFMs is one of the indispensable ingredients for advancing the antiferromagnetic spintronics, it is important to further investigate the magnetoresistive effect in various antiferromagnetic multilayer systems. In this work, we examined the magnetoresistance in Pt/Mn_3Ir and W/Mn_3Ir bilayers. MnIr alloys are one of the most commonly used metallic AFMs in spintronic devices for creating exchange bias [19),20)]. Among various intermetallic alloys of Mn and Ir, $L1_2$-ordered Mn_3Ir is of great interest for the abovementioned novel magnetoresistive behavior owing to the non-collinear chiral magnetic structure [21)].

2. Experimental Procedure

We formed W 6 nm/$Mn_{75}Ir_{25}$ 10 nm/MgO 2nm/W 2 nm and Pt 6 nm/$Mn_{75}Ir_{25}$ 10 nm/MgO 2 nm/W 2 nm on a thermally oxidized Si substrate by magnetron sputtering. The MgO 2 nm/W 2 nm capping layers in both samples are to avoid the sample from oxidation and degradation. The films annealing was performed at $220°C$ for 30 min. We separately confirmed that the Mn_3Ir 10 nm layer in both samples possesses an antiferromagnetic order [22)]. Fig. 1 shows the X-ray diffraction (XRD) of the films before and after the annealing. A distinct difference between the W/Mn_3Ir and the Pt/Mn_3Ir multilayers can be found in the evolution of the (110) superlattice peak of $L1_2$ Mn_3Ir [23)] while (220) peak was buried in the intense (400) peak of Si substrate. The $L1_2$ order is developed in W/Mn_3Ir after annealing while the annealing
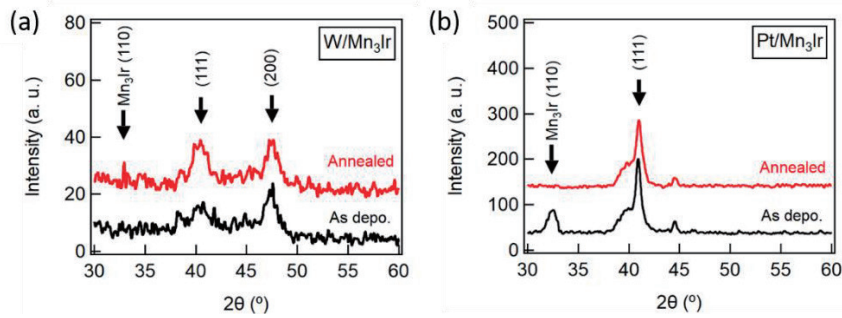
Fig. 1 XRD patterns for (a)W 6 nm/Mn$_3$Ir 30 nm/MgO 2 nm/W 2 nm and (b)Pt 6 nm/Mn$_3$Ir 30 nm/MgO 2 nm/W 2 nm. The black line shows the result of the as deposited film and the red line is the result of the annealed film.
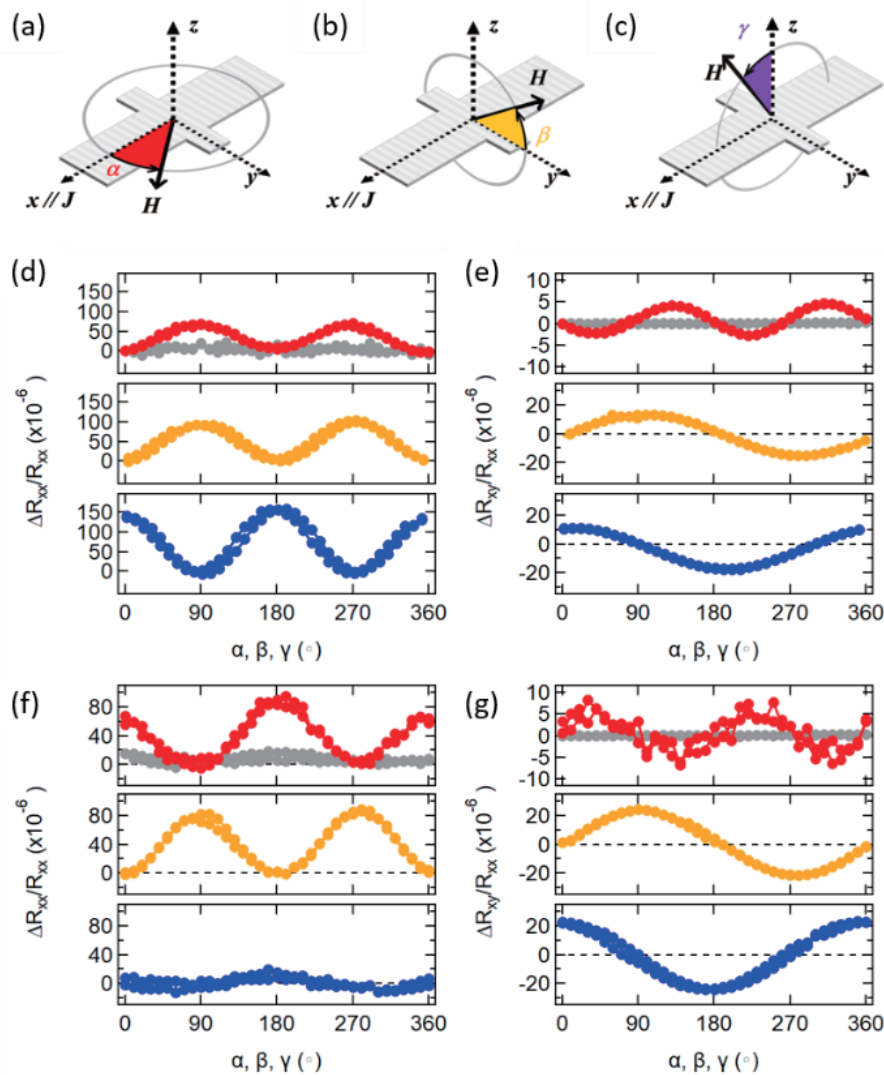
Fig. 2 (a-c) Experimental setup of the electrical transport property measurement and the definition of the coordinate system. H denotes the magnetic field. (d,e) Angular dependence of R_{xx} and R_{xy} under the 9 T field at T = 300 K for the as-deposited (gray data points) and annealed W 6 nm/Mn$_3$Ir 10 nm/MgO 2 nm/W 6 nm (f,g) and for the as-deposited (gray dots) and annealed Pt 6 nm/Mn$_3$Ir 10 nm/MgO 2 nm/W 6 nm.

annihilates the $L1_2$ order in the Pt/Mn$_3$Ir case, indicating that the crystalline symmetry of the underlayer (a (b.c.c.) or β structure for W and f.c.c. for Pt) is important for crystallinity of the Mn$_3$Ir. For electrical measurements, the films were patterned into a 120-µm-long and 30-µm-wide Hall bar structure by a conventional photolithography and Ar ion milling process. The electrical measurements were performed using the Physical Property Measurement System (PPMS-9T, Quantum Design). The longitudinal R_{xx} and transverse
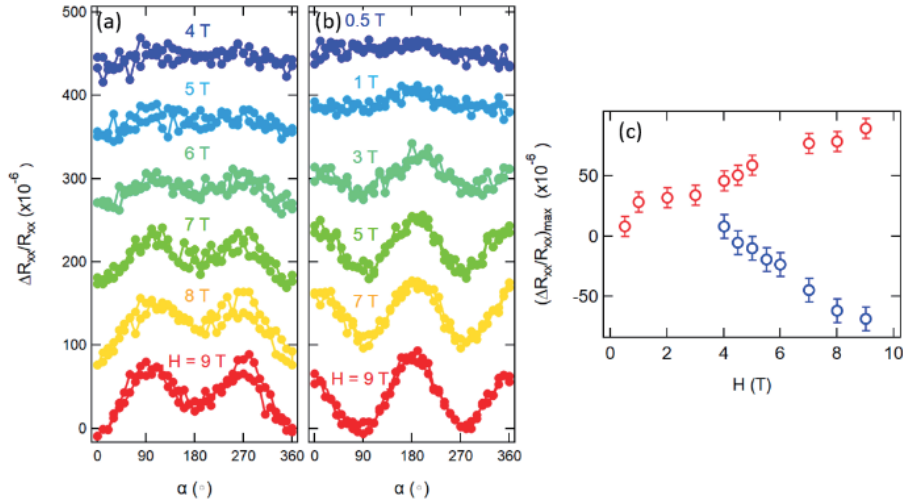
Fig. 3 Field dependence of the magnetoresistive signals in the annealed W/Mn$_3$Ir(a) and Pt/Mn$_3$Ir(b) samples. (c)These magnetoresistance ratios are summarized as a function of magnetic field in red dots(Pt/Mn$_3$Ir) and blue dots(W/Mn$_3$Ir).

R_{xy} resistances were measured with the excitation current of 1 mA ($J \sim 2.1 \times 10^5$ A/cm^2) in a rotating magnetic field with a fixed magnitude ($H = 0 \sim 9$ T). The excitation current flows along x-axis. The definition of the rotating angles: α, β, and γ are indicated in Figs. 2 (a-c).

3. Results

Figures 2 (d-g) show the magnetoresistance ratio $\Delta R_{xx}/R_{xx}$ and $\Delta R_{xy}/R_{xx}$ as functions of α, β, and γ with $H = 9$ T before and after annealing. Both W/Mn$_3$Ir and Pt/Mn$_3$Ir samples did not show any α dependent magnetoresistive behaviors before annealing (as indicated in gray data points in Figs. 2 (d-g)). Measurements in other angles β and γ are omitted. On the other hand, after annealing, appreciable magnetoresistances were observed but the behaviors with respect to the rotating angles differ for the two samples. The most intriguing and distinct differences can be seen in the resistance variation with respect to the rotating angle α which are shifted by $\pi/2$ between the W/Mn$_3$Ir and Pt/Mn$_3$Ir samples. Figure 3 shows the field dependence of $\Delta R_{xx}/R_{xx}$ in the annealed W/Mn$_3$Ir(a) and Pt/Mn$_3$Ir(b) samples. Figure 3 shows the field dependence of $\Delta R_{xx}/R_{xx}$ in the annealed W/Mn$_3$Ir(a) and Pt/Mn$_3$Ir(b) samples. These $\Delta R_{xx}/R_{xx}$ are summarized in Fig.3(c). The $\pi/2$ phase shift is denoted as a different sign of $\Delta R_{xx}/R_{xx}$ between the W/Mn$_3$Ir and Pt/Mn$_3$Ir samples. When $H = 0$ T, only the noise level of the $\Delta R_{xx}/R_{xx}$ was obtained. $\Delta R_{xx}/R_{xx}$ became larger with increasing the magnitude of H. Although the resistance difference between $R_{xx}(\alpha = 0$ degree) and $R_{xx}(\alpha = 180$ degree) is unclear, we can conclude that the saturation magnetic field to manipulate the magnetic moments is over 9 T.

4. Discussion

In order to step into a quantitative argument on these intriguing magnetoresistance behaviors, we firstly consider the change in the longitudinal resistance ΔR_{xx} in these multilayer systems. The derivation of the R_{xx} change due to the SMR and the AMR can start from [4),24)],

$$R_{xx} = \sum^{n} \left(R_0 + \Delta R_{AMR} m_{n,x}{}^2 + \Delta R_{SMR}\left(1 - m_{n,y}{}^2\right)\right) \quad (1)$$

where R_0 is the field independent resistance, and ΔR_{AMR} and ΔR_{SMR} are the resistance change due to AMR and SMR, respectively. $m_{n,x}$ and $m_{n,y}$ are respectively a unit vector along x- and y-axis of the nth magnetic sublattice. Here, we left aside a possible magnetoresistance due to the chiral magnetic structure in absence of a detailed quantitative model but will come back to the point in the later argument. Assuming that the external field is large enough to induce the spin-flopping of the AFM and the magnetic anisotropy energy is negligibly small compared to the exchange energy, Equation (1) leads to ΔR_{xx} depending on the net magnetization vector $\boldsymbol{M}_\parallel$ parallel to the external field and $\boldsymbol{M}_\perp$ perpendicular to the external field, where $\boldsymbol{M}_\parallel$ is regarded as the ferromagnetic order parameter and $\boldsymbol{M}_\perp$ maybe regarded as the antiferromagnetic order parameter, or the Néel vector. Table 1 shows the magnetoresistance ratio $\Delta R_{xx}/R$ considering SMR and AMR for $\boldsymbol{M}_\parallel$ and $\boldsymbol{M}_\perp$. One can notice from the list of the magnetoresistances in Table 1 that the contribution of AMR and SMR can be separated out by having the complete data set for α, β, and γ rotations. Here, the amplitude of the trigonometric functions, A_{FS}, A_{AS}, A_{FA}, and A_{AA} considers the resistance change due to SMR for $\boldsymbol{M}_\parallel$, SMR for $\boldsymbol{M}_\perp$, AMR for $\boldsymbol{M}_\parallel$, AMR for $\boldsymbol{M}_\perp$, respectively. We also derive the change in the

Table 1 Longitudinal resistance change due to SMR and AMR

Rotation	$\Delta R_{xx}^{SMR, M\parallel}/R$	$\Delta R_{xx}^{SMR, M\perp}/R$	$\Delta R_{xx}^{AMR, M\parallel}/R$	$\Delta R_{xx}^{AMR, M\perp}/R$
α	$A_{FS}\cos^2\alpha$	$A_{AS}\sin^2\alpha$	$A_{FA}\cos^2\alpha$	$A_{AA}\sin^2\alpha$
β	$A_{FS}\sin^2\beta$	$A_{AS}\cos^2\beta$	0	0
γ	0	0	$A_{FA}\sin^2\gamma$	$A_{AA}\cos^2\gamma$

Table 2 Transverse resistance change due to SMR and AMR

Rotation	$\Delta R_{xy}^{SMR, M\parallel}/R$	$\Delta R_{xy}^{SMR, M\perp}/R$	$\Delta R_{xy}^{AMR, M\parallel}/R$	$\Delta R_{xy}^{AMR, M\perp}/R$
α	$A_{FS}\sin 2\alpha$	$-A_{AS}\sin 2\alpha$	$A_{FA}\sin 2\alpha$	$-A_{AA}\sin 2\alpha$
β	$A_{FS2}\sin\beta$	0	$A_{FA2}\sin\beta$	0
γ	$A_{FS2}\cos\beta$	0	$A_{FA2}\cos\beta$	0

transverse magnetoresistances ΔR_{xy} in a similar manner starting from the equation [4),24)],

$$R_{xy} = \sum^{n}\left(\Delta R_{AMR}m_{n,x}m_{n,y} + \Delta R_{SMR}m_{n,x}m_{n,y} + \Delta R_{OHE}m_{n,z}\right) \quad (2)$$

where ΔR_{OHE} is the coefficient for the ordinary Hall effect. The contributions to $\Delta R_{xy}/R_{xx}$ by AMR, or planar Hall effect, and SMR are summarized in Table 2 in terms of α, β, and γ rotations. Since the transverse resistance change contains significant amount of the ordinary Hall effect from the Pt layer, which makes the quantitative argument difficult when using $\Delta R_{xy}/R_{xx}$ in the following discussion, we will focus on $\Delta R_{xx}/R_{xx}$ for a quantitative argument.

According to Table 1, considering both SMR and AMR, the amplitude for the rotation α is represented as $(A_{FS} - A_{AS}) - (A_{FA} - A_{AA})$, the amplitude for the rotation β is represented as $A_{FS} - A_{AS}$ and that for the rotation γ is represented as $A_{FA} - A_{AA}$. For the W/Mn₃Ir case, we find $(A_{FS} - A_{AS}) - (A_{FA} - A_{AA})$ = -6.4 x 10⁻⁵, $A_{FS} - A_{AS}$ = 8.4 x 10⁻⁵ and $A_{FA} - A_{AA}$ = -15.4 x 10⁻⁵ (see Figs. 2 (d)), which are not self-consistent indicate that there are additional magnetoresistances we are missing in our consideration in addition to antiferromagnetic order dominant magnetoresistance. On the other hands, for the Pt/Mn₃Ir case, we find $(A_{FS} - A_{AS}) - (A_{FA} - A_{AA})$ = 4.5 x 10⁻⁵, $A_{FS} - A_{AS}$ = 4.3 x 10⁻⁵ and $A_{FA} - A_{AA}$ = -0.9 x 10⁻⁵ (see Figs. 2 (e), which are relatively self-consistent within the error factor of ~ 7 x10⁻⁶. The results of the Pt/Mn₃Ir case is indeed very similar to the previous report which is explained by an uncompensated magnetic moment is induced at Pt/FeMn interface[25]. In other words, a ferromagnetic order parameter is dominant in this case.

Although Mn₃Ir itself is generally robust against 9 T of magnetic field, it is likely that the magnetic moments of Mn₃Ir with the Pt and W underlayer can become manipulated by magnetic field after the annealing. In the case of W/Mn₃Ir, the emergences of the magnetoresistance as well as the additional unknown magnetoresistance seem to be associated with the formation of $L1_2$ ordered structure.

5. Conclusion

In summary, the magnetoresistance in the heavy metal/AFM metal multilayers has been studied. Both Pt/Mn₃Ir and W/Mn₃Ir exhibit appreciable magnetoresistance in a rotating magnetic field with ~ 9 T. Assuming that the AMR and SMR are the relevant magnetoresistive effects in these systems, we found that there is an additional unconventional magnetoresistance contribution in the W/Mn₃Ir. As this additional magnetoresistance is associated with the formation of $L1_2$- Mn₃Ir structure, we speculate that it could be related to the non-collinear antiferromagnetic order.

References

1) T. Jungwirth, X. Marti, P. Wadley, and J. Wunderlich: *Nat. Nanotechnol.*, **11**, 231 (2016).
2) V. Baltz, A. Manchon, M. Tsoi, T. Moriyama, T. Ono, and Y. Tserkovnyak: *Rev. Mod. Phys.*, **90**, 015005 (2018).
3) W. Thomson: *Proc. R. Soc. London*, **8,** 546 (1856).
4) H. Nakayama, M. Althammer, Y.-T. Chen, K. Uchida, Y. Kajiwara, D. Kikuchi, T. Ohtani, S. Geprägs, M. Opel, S. Takahashi, R. Gross, G. E. W. Bauer, S. T. B. Goennenwein, and E. Saitoh: *Phys. Rev. Lett.*, **110**, 206601 (2013).
5) Y.-T. Chen, S. Takahashi, H. Nakayama, M. Althammer, S. T. B. Goennenwein, E. Saitoh, and G. E. W. Bauer: *Phys. Rev. B*, **87**, 144411 (2013).

6) L. Neel: *Nobel Lect.*, (1970).

7) X. Marti, I. Fina, C. Frontera, J. Liu, P. Wadley, Q. He, R. J. Paull, J. D. Clarkson, J. Kudrnovský, I. Turek, J. Kuneš, D. Yi, J. H. Chu, C. T. Nelson, L. You, E. Arenholz, S. Salahuddin, J. Fontcuberta, T. Jungwirth, and R. Ramesh: *Nat. Mater.*, **13**, 367 (2014).

8) T. Moriyama, N. Matsuzaki, K. J. Kim, I. Suzuki, T. Taniyama, and T. Ono: *Appl. Phys. Lett.*, **107**, 122403 (2015).

9) D. Hou, Z. Qiu, J. Barker, K. Sato, K. Yamamoto, S. Vélez, J. M. Gomez-Perez, L. E. Hueso, F. Casanova, and E. Saitoh: *Phys. Rev. Lett.*, **118**, 147202 (2017).

10) G. R. Hoogeboom, A. Aqeel, T. Kuschel, T. T. M. Palstra, and B. J. van Wees: *Appl. Phys. Lett.*, **111**, 052409 (2017).

11) J. Fischer, O. Gomonay, R. Schlitz, K. Ganzhorn, N. Vlietstra, M. Althammer, H. Huebl, M. Opel, R. Gross, S. T. B. Goennenwein, and S. Geprägs: *Phys. Rev. B*, **97**, 014417 (2018).

12) X. Z. Chen, R. Zarzuela, J. Zhang, C. Song, X. F. Zhou, G. Y. Shi, F. Li, H. A. Zhou, W. J. Jiang, F. Pan, and Y. Tserkovnyak: *Phys. Rev. Lett.*, **120**, 207204 (2018).

13) P. Wadley, B. Howells, J. Železný, C. Andrews, V. Hills, R. P. Campion, V. Novák, K. Olejník, F. Maccherozzi, S. S. Dhesi, S. Y. Martin, T. Wagner, J. Wunderlich, F. Freimuth, Y. Mokrousov, J. Kuneš, J. S. Chauhan, M. J. Grzybowski, A. W. Rushforth, K. W. Edmonds, B. L. Gallagher, and T. Jungwirth: *Science*, **351**, 587 (2016).

14) S. Y. Bodnar, L. Šmejkal, I. Turek, T. Jungwirth, O. Gomonay, J. Sinova, A. A. Sapozhnik, H.-J. Elmers, M. Kläui, and M. Jourdan: *Nat. Commun.*, **9**, 348 (2018).

15) M. Meinert, D. Graulich, and T. Matalla-Wagner: *Phys. Rev. Appl.*, **9**, 64040 (2017).

16) X. F. Zhou, J. Zhang, F. Li, X. Z. Chen, G. Y. Shi, Y. Z. Tan, Y. D. Gu, M. S. Saleem, H. Q. Wu, F. Pan, and C. Song: *Phys. Rev. Appl.*, **9**, 054028 (2018).

17) H. Chen, Q. Niu, and A. H. MacDonald: *Phys. Rev. Lett.*, **112**, 017205 (2014).

18) S. Nakatsuji, N. Kiyohara, and T. Higo: *Nature*, **527**, 212 (2015).

19) J. Nogués and I. K. Schuller: *J. Magn. Magn. Mater.*, **192**, 203 (1999).

20) Y. Y. Wang, C. Song, J. Y. Zhang, and F. Pan: *Prog. Nat. Sci. Mater. Int.*, **27**, 208 (2017).

21) I. Tomeno, H. N. Fuke, H. Iwasaki, M. Sahashi, and Y. Tsunoda: *J. Appl. Phys.*, **86**, 3853 (1999).

22) We did field cooled with an external field of 0.3 T in separate W(6 nm)/Mn$_3$Ir(10 nm)/FeCoB(4 nm) and Pt(6 nm)/Mn$_3$Ir(10 nm)/FeCoB(4 nm) samples to confirm its antiferromagnetic order by observing exchange bias. The magnitude of the exchange bias were estimated from the planar Hall effect by using a fitting function that we reported before in K. Oda, T. Moriyama, M. Kawaguchi, M. Kamiya, K. Tanaka, K.-J. Kim, and T. Ono: *Jpn. J. Appl. Phys.,* **55**, 070304 (2016). As a result, exchange bias in the former structure showed 0.0106 T while in latter structure was 0.0416 T.

23) A. Kohn, A. Kovács, R. Fan, G. J. McIntyre, R. C. C. Ward, and J. P. Goff: *Sci. Rep.*, **3**, 2412 (2013).

24) T. R. Mcguire and R. I. Potter: *IEEE Trans. Magn.*, **11**, 1018 (1975).

25) Y. Yang, Y. Xu, X. Zhang, Y. Wang, S. Zhang, R. W. Li, M. S. Mirshekarloo, K. Yao, and Y. Wu: *Phys. Rev. B*, **93**, 094402 (2016).

<Paper>

High coercivity and resolution FePt・MgO-coated tip for imaging the magnetic field of perpendicular magnetic write head by alternating magnetic force microscopy (A-MFM)

F. Zheng[1,2], S. Yoshimura[3], S. Yasui[3], G. Egawa[3], and H. Saito[3]

[1]Venture Business Laboratory, Akita University, *Tegata Gakuen-machi 1-1, Akita 010-8502, Japan*
[2]School of Physics and Electronic-Electrical Engineering, Ningxia University, *Yinchuan 750021, China*
[3]Research Center for Engineering Science, Graduate School of Engineering Science, Akita University,
Tegata Gakuen-machi 1-1, Akita 010-8502, Japan

High coercivity FePt・MgO films were successfully synthetized on cone-shape Si tips in a very high frequency (VHF) plasma irradiation-assisted magnetron sputtering system to prepare the MFM tips for evaluation of the AC magnetic field of perpendicular magnetic write head at high write current. Alloying with MgO significantly enhanced the coercivity of the magnetic coating due to the isolation of FePt grains by MgO. As a result, a high coercivity close to 20 kOe was achieved. The AC magnetic field images of the perpendicular magnetic write head at high write current were taken on alternating MFM (A-MFM) by this tip. A clear amplitude image with a strong signal at the main pole position was observe compared to the pure FePt layer-coated tip, which gave a blurry image and very small amplitude. Fourier analysis of the images obtained by this kind of FePt・MgO tip gives a spatial resolution of about 15 nm in air atmosphere. It is clear that the cone-shape FePt・MgO-coated MFM tip with a coercivity higher than the magnetic field to be measured is effective and capable for measuring the high AC magnetic field for an HD perpendicular magnetic write head at a very high write current.

Key words: high-coercivity and high-resolution FePt・MgO-coated tip, very high frequency (VHF) plasma irradiation, perpendicular magnetic write head, alternating magnetic force microscopy (A-MFM)

1. Introduction

Magnetic force microscopy (MFM) is an effective scanning probe for investigation of the magnetic domain structures of magnetic materials in nanoscale such as magnetic recording media because of its high spatial resolution of the static magnetic field[1]. The MFM tip is the most important key element to detect and image the surficial magnetic signal of an object. A high coercivity magnetic tip is one of the essential parameters for MFM imaging. Commercially-available MFM tip is usually an atomic force microscopy (AFM) tip coated with a thin CoCrPt film. There have been many efforts to prepare MFM tips such as synthetic antiferromagnetic coating with sandwich structures[2,3], focused ion beam (FIB) trimming[4-6], carbon nanotubes coated with magnetic films[7,8]. Hard magnetic coatings of Fe-Pt[9-13], Fe-Pd[13,14], Co-Pt[15-18], Sm-Co[19] were used for the preparation of MFM tips to image large magnetic field. In addition to the MFM tip, the methodology of MFM itself is also critical. We have developed a new MFM imaging method for characterization of AC magnetic field. We named it as alternating MFM (A-MFM)[20]. The A-MFM uses a frequency modulation (FM) of the cantilever oscillation by applying an AC magnetic field on a mechanically oscillated tip. This can allow us to measure the perpendicular component of the AC magnetic field with respect to the sample surface. Previously, we used in-house-coated FePt tips with high-coercivity to image the

AC magnetic field of a perpendicular magnetic write head having a one-sided trailing shield on our A-MFM set up[21,22,23]. The spatial resolution was estimated to be 15 nm (a lift height of 1 nm and AC current with a zero-to-peak amplitude of 20 mA). However, this tip failed to characterize the AC magnetic field of the head having three surrounding shields when a large write current which generates a large magnetic field bigger than the coercivity of the FePt coating on the tip. To estimate the distribution of magnetic field from the head having three surrounding shields, MFM tip with symmetry shape for the magnetic charge and with high coercivity magnetic film is effective. We had reported the cone-shaped MFM tip with symmetry for the magnetic charge to get a MFM image without distortion[24]. We also had reported that coercivity of the FePt coated MFM tip is lower than the magnetic field generated by the head having three surrounding shields with large head current[24].

We deposited FePt・MgO films on the tip by VHF plasma irradiation-assisted magnetron sputtering in order to increase the coercivity of magnetic FePt film. The MgO[25] was used for isolation of FePt grains. The VHF plasma irradiation enhanced the $L1_0$ FePt phase during sputtering[26]. The new FePt・MgO MFM tip with very high coercivity was used for observation of AC magnetic image of perpendicular magnetic write head in this work.
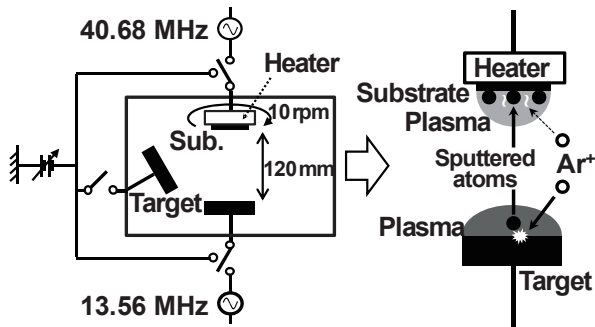
Fig. 1 Schematic image of VHF irradiation assisted ultra-high vacuum sputtering system.

2. Experimental Procedure

FePt・MgO films with the total thickness of 20 nm were prepared onto Si substrates which had thermally-oxidized surface for the purpose to check their structure and magnetic properties. The FePt・MgO films were deposited in two different paths: one path was to sputter a composite target where many pieces of thin MgO plates were placed on the top of a $Fe_{50}Pt_{50}$ target; another path was to co-sputter both $Fe_{50}Pt_{50}$ and MgO targets. The volume fraction (Vol.%) of MgO in the final film was adjusted by changing the numbers of MgO thin plates on the $Fe_{50}Pt_{50}$ target, the sputtering power, and/or the target-to-substrate (T-S) distance. During the sputtering, the VHF plasma irradiation[26] was fixed at 40.68 MHz with the electric power (P_{VHF}) of 5 ~ 20 W as shown in Fig. 1. After sputtering, the FePt・MgO films were annealed at 750 ℃ in a rapid thermal annealing (RTA) system for 10 minute. The crystalline characteristics of the films were analyzed by x-ray diffraction (XRD). The magnetic properties were measured by a vibrating sample magnetometer (VSM). The made-in-house MFM tips with a cone-shaped Si tip (SSISC, Team Nanotec Co. Ltd.) consisted of a very thin SiO_2 layer formed by plasma oxidation and a layer of the magnetic FePt・MgO (20 - 40 nm) film which were prepared under the same sputtering a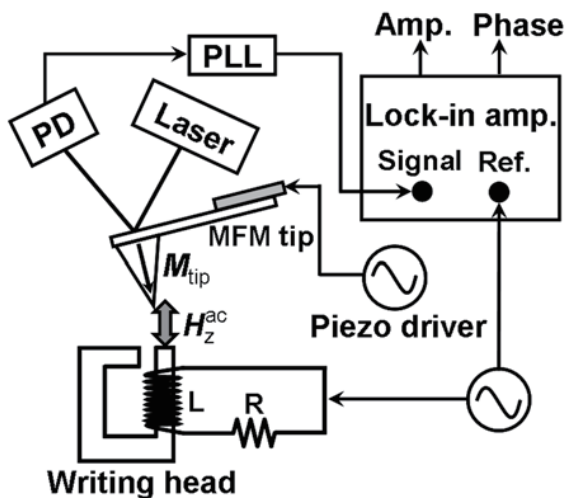nd post-annealing conditions. SiO_2 layer was used to prevent interdiffusion between the magnetic film and Si tip. Before measurement, the MFM tips were magnetized to saturation along the tips axis, which means that the magnetization direction of the tips was vertical to the sample surface.

The A-MFM runs were carried out based on a conventional scanning probe microscope (JSPM-5400 (JEOL Ltd.)) in an air atmosphere. Figure 2 shows a scheme of the A-MFM. A lock-in amplifier and a phase-locked loop (PLL) circuit were used for the AC magnetic field measurement in the A-MFM[21],[22],[23]. The cantilever was oscillated by using a piezoelectric element. The resonant frequency of the cantilever with the MFM tip was approximately 256 kHz. The oscillation frequency (f_c) of the piezoelectric element was about 250 kHz which is close to the resonant frequency of the tip, and the value of Q was around 500. The AC magnetic field was measured on the lift mode after topographic characterization. The lift height was 8 nm or 1 nm. The good spatial resolution was obtained at the lift height of 1 nm.

An advanced perpendicular magnetic write head having three surrounding shields was used for evaluation. In comparison with the magnetic write head having a one-sided trailing shield[21],[22],[23], this kind of write head can generate focused magnetic field for high recording density. The write head was run by a sinusoidal AC current with a zero-to-peak amplitude of 20 - 40 mA and a frequency (f_m) of 100 Hz.

3. Results and Discussions

Figure 3 shows θ-2θ XRD patterns of FePt, and FePt・MgO (16 Vol.% MgO) films without/with VHF plasma irradiation power of 15 W. All of the films show strong FePt(111) peak, which means the deposited FePt-based films have preferred (111)-texture. Due to the lowest interfacial energy of FePt(111) plane, the FePt film deposited on amorphous SiO_2 substrate can have a
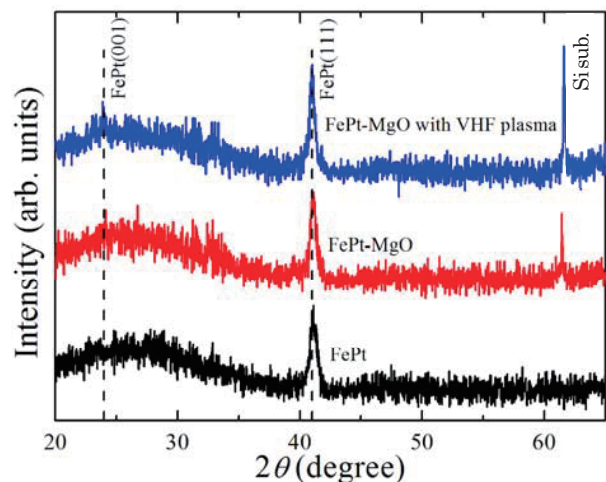

Fig. 2 Schematic of A-MFM system.

Fig. 3 θ-2θ XRD patterns of FePt and FePt・MgO films.

(111)-favor texture growth. In Fig.3 you cannot see a clear (001) peak, but the sputtering film with VHF plasma irradiation shows an enhanced (111) peak intensity, compared to the films without VHF plasma irradiation. The integral intensity of FePt(111) was 4853, 5155, and 6763, for the films of FePt, FePt・MgO, and FePt・MgO with VHF plasma, respectively. In our previous study[26], a VHF plasma irradiation during sputtering deposition can effectively accelerate crystallization and atom ordering. It is believed that the VHF plasma irradiation can also accelerate the crystallization and ordering of $L1_0$ FePt phase. As we know, the high magnetic anisotropy of FePt films can be obtained in the chemically ordering state, which can lead to high coercivity.

An in-plane easy axis of magnetization of the magnetic coating on is preferred for MFM tip preparation. Figure 4 shows the dependence of the in-plane coercivity of FePt・MgO films on the volume fraction of MgO. The inset shows hysteresis loops of FePt and $(FePt)_{84}・(MgO)_{16}$ film (in Vol.%), respectively. The coercivity rises from 9.2 kOe to 17.0 kOe when MgO's volume percentage in FePt・MgO film increases from 0 to 35 Vol.%. It is obvious that MgO addition to the FePt film significantly enhance the coercivity of the film. This is believed that the MgO's effect of isolation of FePt grains attributes to increased coercivity like the other kinds of element additives such as SiO_2[27], C[28], TiO_2[29,30] added to FePt-base films.

Figure 5 shows the in-plane coercivity of FePt・MgO films versus the VHF plasma irradiation power. The inset shows hysteresis loops of $(FePt)_{84}・(MgO)_{16}$ film with VHF plasma irradiation power of 15 W. As shown in the figure, the coercivity gradually increases from 14.5 kOe to 15.9 kOe when VHF power changes from 5 W to 15 W. And then coercivity drops to 15.2 kOe as VHF power goes up to 20 W. The VHF bias is considered to have two effects: 1) the enhancement of atoms/ molecules'
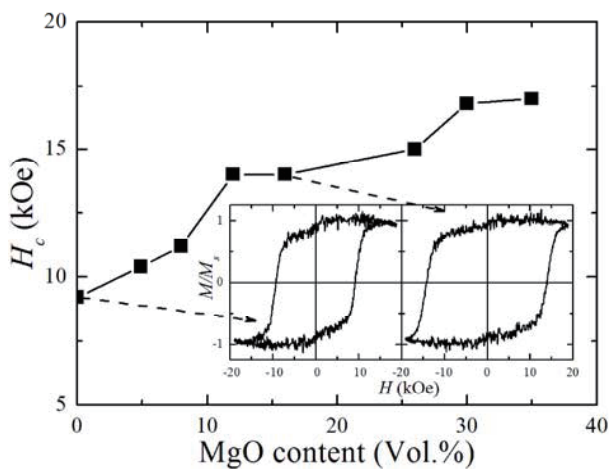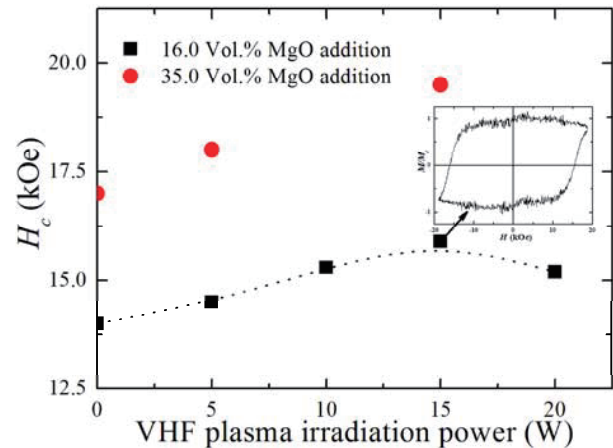
Fig. 5 Dependence of the in-plane coercivity of FePt・MgO films on the VHF plasma irradiation power. The inset is hysteresis loop of $(FePt)_{84}・(MgO)_{16}$ with VHF plasma irradiation power of 15 W.

mobility for ordering and 2) the ion bombardment on film during sputtering. The effect 1) of VHF bias is taking place to increase coercivity when the VHF power is low. This is supported by XRD measurement shown in Figure 3. The effect 2) of VHF bias becomes dominant and enhances disordering atoms/ molecules of FePt in the film so to reduce in-plane coercivity when VHF power is high. The highest in-plane coercivity achieved at the composition of 16 Vol.% MgO under a proper VHF plasma irradiation during sputtering suggests the importance of both FePt atoms ordering and MgO molecules' isolation effects for making high coercivity films. This is also supported by the $(FePt)_{65}・(MgO)_{35}$ film's behavior as shown in Figure 5. It is clearer that an optimized VHF bias power (enhancement of FePt ordering) and more MgO concentration (more isolations of FePt grains) can give higher in-plane coercivity (more than 20 kOe) to FePt films.

The two kinds of MFM tips with FePt and $(FePt)_{84}・(MgO)_{16}$ coatings were fabricated for evaluation of the AC magnetic field of a write head having three surrounding shields. The $(FePt)_{84}・(MgO)_{16}$ film was formed under a VHF plasma irradiation power of 15 W. The nominal thickness of both FePt-base coatings was 40 nm. Here, we discussed the evaluation of magnetic properties of MFM tips by using pulsed magnetic field magnetic force microscope[31], and also estimated the coercivity of MFM tips[32]. The measured coercivity of FePt・MgO MFM tips was closed to the values of FePt・MgO films. The A-MFM measurement was taken at a lift height of 8 nm. The head write current was 40 mA. Figs.6 (a) shows the topographic image of the write head around the main pole area.

The amplitude images of AC magnetic field generated from the write head measured by the FePt-coated tip and $(FePt)_{84}・(MgO)_{16}$-coated tip having an coercivity of 15.9 kOe is clear and has high amplitude signal at the main pole position. In contrast, the amplitude image measured
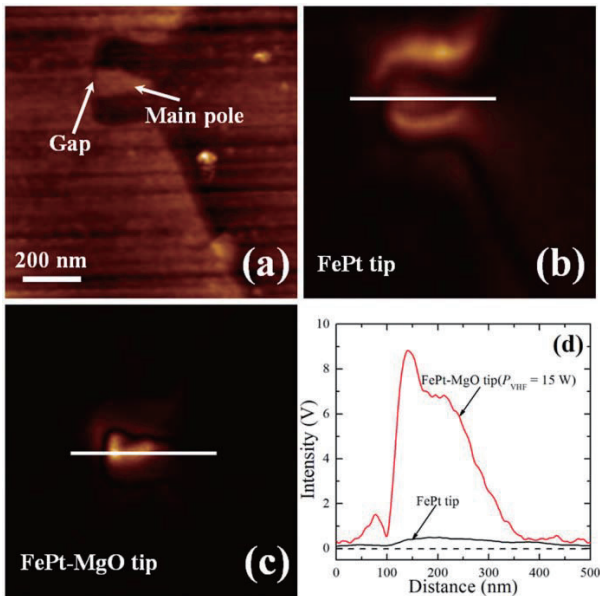
Fig. 4 The in-plane coercivity versus MgO volume fraction in FePt・MgO films. The inset shows hysteresis loops of FePt and $(FePt)_{84}・(MgO)_{16}$ film.

Fig. 6 (a) is a topographic image, (b) and (c) are amplitude images of the AC magnetic field for the magnetic write head, and (d) is down track line profiles of amplitude signal of the white line in (b) and (c). The images in (b) and (c) are obtained using the FePt- and FePt・MgO-coated tips, respectively.

by FePt-coated tip having a coercivity of 9.2 kOe is unclear and has very low amplitude signal at the main pole position. In contrast, the amplitude image measured by FePt-coated tip having a coercivity of 9.2 kOe is unclear and has very low amplitude signal at the main pole position. These results indicate that the FePt・MgO-coated tip with a coercivity higher than the field generated from the write head can effectively image the AC magnetic field without signal decay because the high coercivity can suppress the tip's magnetization rotation. In one word, the clear amplitude image is obtained by the FePt・MgO-coated tip with a high coercivity in this case.

In order to clarify and enhance the spatial resolution of our High coercivity MFM tips, a 20 nm-thick $(FePt)_{84}\cdot(MgO)_{16}$-coated tip was fabricated under the same conditions as above. Figs.7 (a) and (b) are amplitude and phase images of the AC magnetic field for a magnetic write head measured by this tip. The lift height was fixed at 1 nm. The head write current was also 40 mA. Figs.7 (c) and (d) are down track line profiles of amplitude and phase signal over the white line locations in Figs.7 (a) and (b), respectively. The clear amplitude image and high amplitude signal at the main pole position are achieved again. This further indicates that the MFM tip with a coercivity higher than the AC magnetic field to be measured can effectively image the AC magnetic field without signal decay. The phase image near the main pole region was measured in the same scan. The phase difference between the bright and dark area was about 180° as shown in the line profile of Figs.7 (d). When the direction of the perpendicular AC magnetic
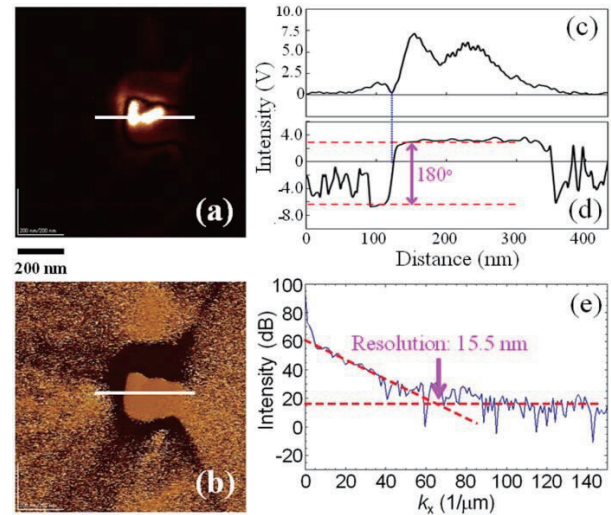

Fig. 7 (a) amplitude and (b) phase images of the AC magnetic field for the magnetic write head measured by 20 nm $(FePt)_{84}\cdot(MgO)_{16}$-coated tip. (c) and (d) are down track line profiles of amplitude and phase signal of the white line in (a) and (b), respectively. (e) is the spatial resolution result of the amplitude image.

field is reversed from $H_z{}^{ac}$ to $-H_z{}^{ac}$, the input signal of a lock-in amplifier changes in the following way.

$$-H_z^{ac}\cos(\omega_m t) = H_z^{ac}\cos(\omega_m t + \pi) \qquad (1)$$

Therefore, the areas with bright and dark colors in the phase image correspond to the opposite directions of perpendicular magnetic field. In another words, the phase image gives the polarity of the AC magnetic field vertical to the surface measured.

Figs.7 (e) shows the spatial resolution of the amplitude imaging. The resolution is obtained from Fourier transformation of the amplitude scan line around main pole. The details of this calculation were described in reference papers[21]. The spatial resolution of amplitude imaging is 15.5 nm in this case. This value is very close to the result of our previous study. Here, the coercivity of FePt・MgO films maintains more than 15 kOe, even if its film thickness is reduced to 10 nm. Therefore, the FePt・MgO MFM tip with the thin FePt・MgO film is expected to be useful for improvement of the spatial resolution owing to the reduction of diameter of end point of the tip. In consideration of that the head structure having three surrounding shields and a high write current of 40 mA, the high coercivity FePt・MgO-coated MFM tip is so successful in imaging such high magnetic field from the head.

4. Conclusion

In-plane (111)-textured FePt and FePt・MgO films were deposited on pre-oxidized Si substrates and Si tips for the study of the effect of coercivity of magnetic coatings on MFM tips. The coercivity of FePt・MgO coatings rises when increasing the MgO's concertation in FePt・MgO alloys under an optimized VHF plasma

irradiation power. The high coercivity of FePt・MgO films is believed due to the isolation of FePt grains by MgO and enhancement of atomic ordering of FePt by a VHF bias. A clear amplitude image and high amplitude signal at the main pole position were observed by using this High coercivity FePt・MgO tip. The spatial resolution of this type of MFM tip is around 15 nm. As simply speaking, the cone-shape FePt・MgO-coated MFM tip with a coercivity higher than the magnetic field to be measured is effective and capable to measure the high AC magnetic field for a perpendicular magnetic write head at a very high write current.

References

1) D. Rugar, H. J. Mamin, P. Guethner, S. E. Lambert, J. E. Stern, I. Mc-Fadyen, and T. Yogi: *J. Appl. Phys.*, **68**, 1169 (1990).

2) Y. H. Wu, Y. T. Shen, Z. Y. Liu, K. B. Li, and J. J. Qiu: *Appl. Phys. Lett.*, **82**, 1748 (2003).

3) N. Amos, R. Ikkawi, R. Haddon, D. Litvinov, and S. Khizroev: *Appl. Phys. Lett.*, **93**, 203116 (2008).

4) Z. Y. Liu, Y. Dan, J. J. Qiu, and Y. H. Wu: *J. Appl. Phys.*, **91**, 8843 (2002).

5) L. Gao, L. P. Yue, T. Yokota, R. Skomski, S. H. Liou, H. Takahoshi, H. Saito, and S. Ishio: *IEEE Trans. Magn.*, **40**, 2194 (2004).

6) C. Hyun, A. K. H. Lee, and A. d. Lozanne: *Nanotechnology*, **17**, 921 (2006).

7) Z. F. Deng, E. Yenilmez, J. Leu, J. E. Hoffman, E. W. J. Straver, H. J. Dai, and K. A. Moler: *Appl. Phys. Lett.*, **85**, 6263 (2004).

8) F. Wolny, T. Mühl, U. Weissker, K. Lipert, J. Schumann, A. Leonhardt, and B. Büchner: *Nanotechnology*, **21**, 435501 (2010).

9) Y Rheem, H Saito, and S Ishio: *IEEE Trans. Magn.*, **41**, 3793 (2005).

10) I.C. Chen, L.H. Chen, A. Gapin, S. Jin, L. Yuan, and S.H. Liou: *Nanotechnology*, **19**, 075501 (2008).

11) N. Amos, A. Lavrenov, R. Fernandez, R. Ikkawi, D. Litvinov, and S. Khizroev: *J. Appl. Phys.*, **105**, 07D526 (2009).

12) N. Amos, R. Fernandez, R.M. Ikkawi, M. Shachar, J.M. Hong, B.S. Lee, D. Litvinov, and S. Khizroev: *IEEE Magn. Lett.*, **1**, 6500104 (2010).

13) S. Ishihara, M. Ohtake, and M. Futamoto: Thin Solid Films, **546**, 205 (2013).

14) S. Ishihara, M. Ohtake, and M. Futamoto: *EPJ Web Conf.*, **40**, 08003 (2013).

15) S.H Liou and Y.D Yao: *J. Magn. Magn. Mater.*, **190**, 130 (1998).

16) S. Ishihara, T. Hagami, K. Soneta, M. Ohtake, and M. Futamoto: *J. Magn. Soci. Jpn.*, **37**, 56 (2013).

17) S. Ishihara, M. Ohtake, and M. Futamoto: *J Magn. Soci. Jpn.*, **37**, 255 (2013).

18) S. Ishihara, M. Ohtake, and M. Futamoto: *EPJ Web Conf.*, **75**, 06007 (2014).

19) V. Neu, T. Sturm, S. Vock, and L. Schultz: *IEEE International Magnetics Conference (INTERMAG Europe 2014)*, EG-6 (2014).

20) H. Saito, H. Ikeya, G. Egawa, S. Ishio, and S. Yoshimura: *J. Appl. Phys.*, **105**, 07D524 (2009).

21) W. Lu, Z. H. Li, K. Hatakeyama, G. Egawa, S. Yoshimura, and H. Saito: *Appl. Phys. Lett.*, **96**, 143104 (2010).

22) W. Lu, K. Hatakeyama, G. Egawa, S. Yoshimura, and H. Saito: *IEEE Trans. Magn.*, **46**, 1479 (2010).

23) H. Saito: *Magune*, **11**, 217 (2016).

24) S. Yoshimura, F. Zheng, S. Yasui, G. Egawa, and H. Saito: *J. Magn. Soc. Jpn.*, **42**, 5 (2018).

25) Z. Zhang, K. Kang, Kyongha, and T. Suzuki: *IEEE Trans. Magn.*, **40**, 2455 (2004).

26) S. Yoshimura, H. Kobayashi, G. Egawa, H. Saito, and S. Ishida: *J. Appl. Phys.*, **109**, 07B751 (2011).

27) C. P. Luo and D. J. Sellmyer: *Appl. Phys. Lett.*, **75**, 3162 (1999).

28) J. S. Chen, B. C. Lim, J. F. Hu, B. Liu, G. M. Chow, and G. Ju: *Appl. Phys. Lett.*, **91**, 132506 (2007).

29) Y. F. Ding, J. S. Chen, B. C. Lim, J. F. Hu, B. Liu, and G. Ju: *Appl. Phys., Lett.*, **93**, 032506 (2008).

30) C. J. Jiang, J. S. Chen, J. F. Hu, and G. M. Chow: *J. Appl. Phys.*, **107**, 123915 (2010).

31) Y. Zheng, S. Yoshimura, G. Egawa, F. Zheng, Y. Kinoshita and H. Saito: *J. Phys. D: Appl. Phys.*, **48**, 335006, (2015).

32) F. Zheng, S. Yoshimura, Y. Zheng, G. Egawa, Y. Kinoshita, and H. Saito: IEEE International Magnetics Conference (INTERMAG EUROPE 2014), CS-17 (2014)

<Paper>

Evaluation on Edge-supported Magnetic Levitation Apparatus for Thin Steel Plates

Y. Oda, Y. Ito, K. Okuno, M. Kida, T. Suzuki,
A. Endo, T. Narita*, H. Kato* and H. Moriyama*

Course of Mechanical Engineering, Graduate School of Tokai Univ., *4-1-1 Kitakaname, Hiratsuka-shi, Kanagawa 259-1292, Japan*
* Department of Prime Mover Engineering, Tokai Univ.

Grasping and conveying an object, by utilizing the frictional force generated by contact is performed in various processes in the manufacturing line for an industrial product. The deterioration of the surface quality due to these contacts is a problem. As a solution to this problem, a noncontact transport of steel plates, using electro-magnetic force, has been proposed. However, in these systems, electromagnets are installed vertically. In this method, if the steel plate is thin and does not have sufficient flexural rigidity, it is difficult to add a suspension force for levitation over the entire steel plate. In order to solve this problem, we proposed an edge supported electromagnetic levitation system for flexible steel plates using electromagnets installed horizontally. In order to verify the effectiveness of the proposed system we constructed a prototype of an edge-supported type magnetic levitation system, which applied electromagnetic force only from the horizontal direction of the steel plate. Consequently, we carried out levitation experiment and discussed characteristics of horizontal positioning and levitation suspension.

Key words: electromagnetic levitation, thin steel plate, vibration control, magnetic field

1. Introduction

Thin steel plates are used in many industrial products and their transportation take place by contact with a large number of rollers in the manufacturing process. Recently, the demand of high quality steel is increasing. Therefore, the deterioration of the surface quality is a problem for this type of contact transportation. To solve this problem, the application of a magnetic levitation technology to a non-contact transport system is actively being studied[1-5]. The authors' research group had installed electromagnets not only vertically but also horizontally. Vertical electromagnets' levitation is applying tension to the steel plate edges. We have confirmed that horizontal electromagnets improve levitation stability in thin steel plates with extremely low flexural rigidity[6-7]. Furthermore, they help realize advanced levitation control systems considering the steel plate deflection as well as the vibration characteristics. Levitation control using only electromagnets from the edge direction is important. Hitherto, we have confirmed the characteristics of the suspension force of the edge direction electromagnet acts on the steel plate by experiment and analysis[8]. In this study, we made a prototype edge supported electromagnetic levitation system based on these characteristics and we discuss the levitation characteristics.

2. Edge Supported Electromagnetic Levitation System

Figure 1 shows a schematic illustration of the newly made edge supported electromagnetic levitation system. Figure 2 shows the placement of the electromagnet and the sensor view from the top. As Fig. 2 shown, the vertical direction is defined as Z direction, the longitudinal
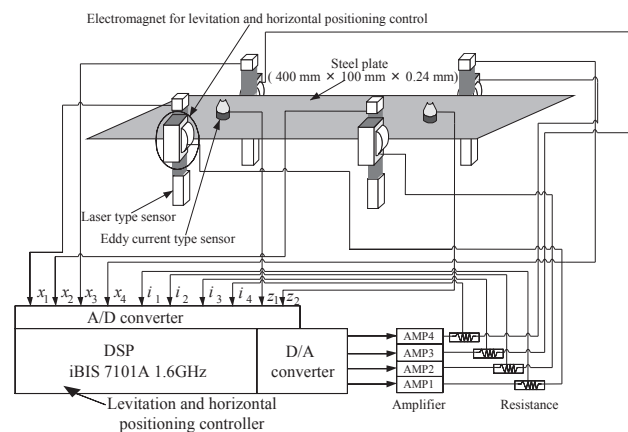

Fig. 1 Edge supported levitation system for steel plate using only electromagnets installed horizontally.

direction of steel plate is defined as Y direction and the transverse direction is defined as X direction. Figure 3 shows a photograph of the electromagnetic levitation system during the levitation of a steel plate. The levitating object is a rectangular galvanized steel plate (material SS400) whose length is 400 mm, width is 100 mm, and thickness is 0.24 mm. In the electromagnetic levitation system, as shown in Fig. 4, two electromagnets facing each other are installed in the longitudinal direction near the edge of the thin steel plate. The attractive force of the electromagnets installed in the X direction, near the edge of the steel plate, perform non-contact positioning control. In a previous study[7], we calculated the deflection shape using magnetic field analysis and the finite difference method. The electromagnets are installed at such position to minimize
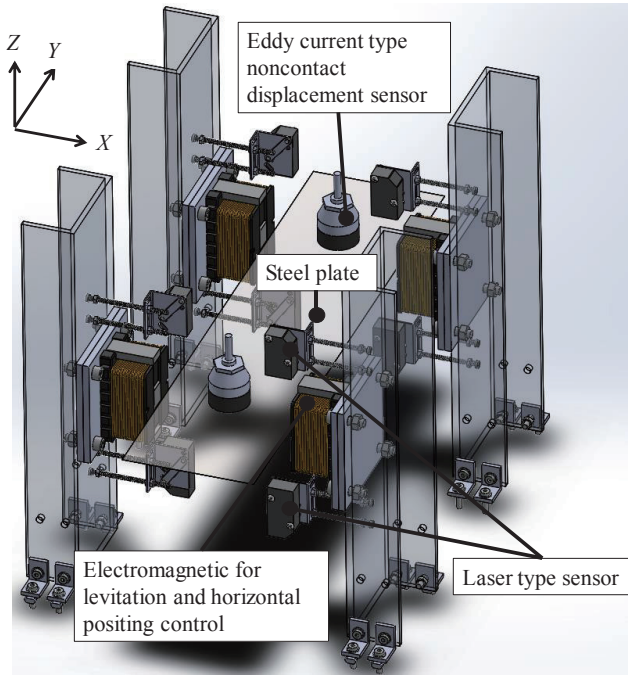
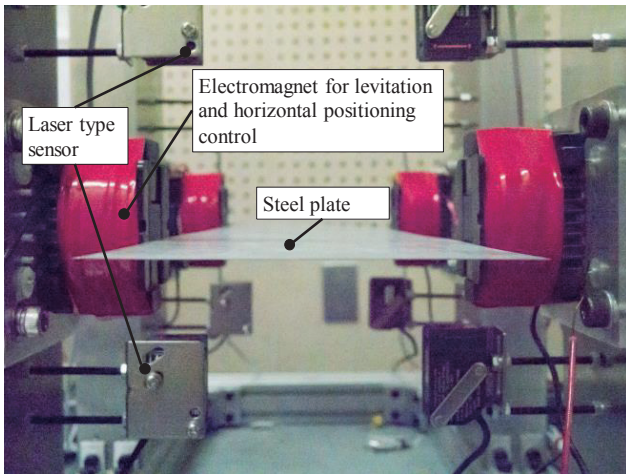**Fig. 2** Schematic illustration of the edge supported levitation system.

Fig. 3 Photograph of the electromagnetic levitation system.

deflection and to expect stability on the steel plate. A laser-type sensor, which measure the displacement by the cut-off amount of a belt-like laser beam manufactured by KEYENCE was used to measure the horizontal displacement in X direction of the edge of the steel plate. Thereby, the steel plate is controlled by non-contact positioning by the electromagnets at a distance of 5 mm from the edge of the steel plate. Furthermore, the control law is calculated by detecting the current in each electromagnet from the measured external resistance and, subsequently, inputting eight measurement values into a digital signal processor of an A/D converter. The core, shown in Fig. 5, is an E-type electromagnet, and the material is ferrite. The electromagnet's core is an enamel wire of 0.5 mm diameter wound around it 1005 times. For evaluating the
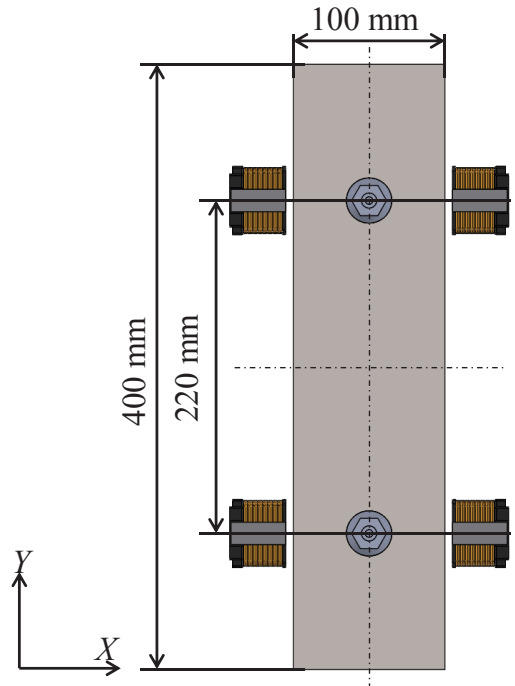

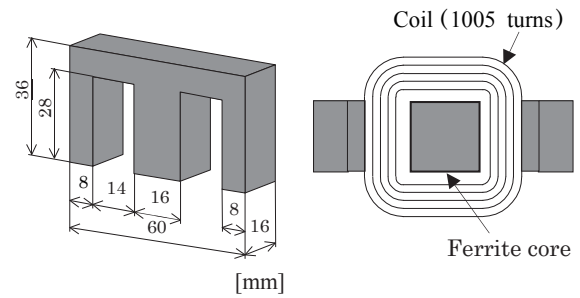**Fig. 4** Placement of electromagnet and displacement field sensor.

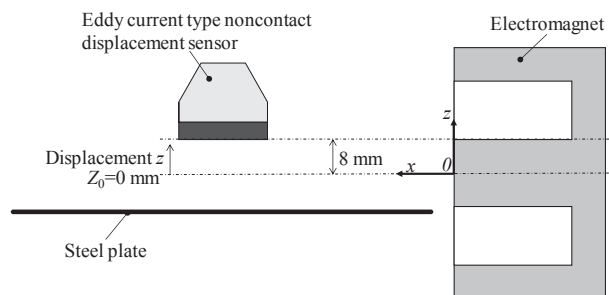**Fig. 5** Configuration of the electromagnet.

Fig. 6 Position of eddy current type noncontact displacement sensor.

levitating state of the steel plate, a vertical direction displacement sensor was installed as shown in Fig. 4 and Fig. 6. An eddy current non-contact displacement sensor manufactured by SENTEC was used. To consider the characteristic of suspension force generated by electromagnet, electromagnetic analysis was carried out. The analytical model is consisting of one electromagnet and steel plate (400 mm × 100 mm). The suspension force
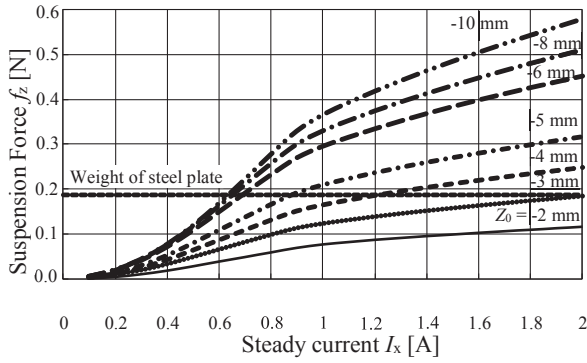
Fig. 7 Relationship between the vertical attractive force f_z for each displacement Z_0.
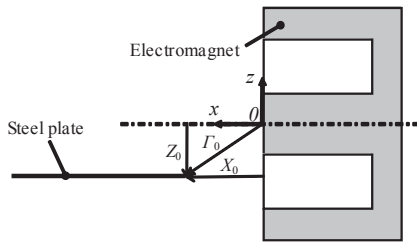

Fig. 8 Coordinate of static levitating steel plate.

Fig. 9 Schematic illustration of attractive force of electromagnets.

was analyzed in the case that the steady current and vertical displacement of the steel plate is changed. Figure 7 shows the relationship between the vertical direction suspension force and the steady current in the electromagnet, which is obtained from the magnetic analysis. Each data shows the suspension force that was applied on the steel plate in the z direction from the center of the electromagnet core. The dashed line (0.18 N) in the figure means the quarter weight of the steel plate, which is equal to suspension force for levitation generated by one electromagnet in this system. It is possible to levitate the steel plate at a steady current value that corresponds to the steel plate's weight.

3. Control Model of Edge Supported Electromagnetic Levitation System

3.1 Equation of motion for levitated thin steel plate

As shown in Fig. 8, edge of the steel plate is displaced from electromagnet surface in the x direction x_{sp} [mm] and from center of electromagnet in the z direction z_{sp} [mm], when the steel plate is levitate horizontally in equilibrium state. Attractive force by magnetic field from installed electromagnet is generated near edge of the steel plate[8]. From the previous study, in the electromagnet core and the steel plate size used in this study, the suction force is regarded generated in one point in the edge of steel plate. We confirmed that the

attractive force generated on the steel plate by the electromagnet is generated toward the tip of center convex part of the electromagnet core. Attractive force F generated on the steel plate is shown by the following equation.

$$F = \frac{L_{\text{eff}}}{2} \frac{i^2}{\gamma_{\text{sp}}^2} \tag{1}$$

Where i_{em} is coil current [A], γ_{sp} is distance from center of electromagnet to edge of the steel plate [mm], $L_{\text{eff}} / \gamma_{\text{sp}}$ is a constant corresponding to the effective magnetic flux of the electromagnet. It is also,

$$\gamma_{\text{sp}} = \sqrt{x_{\text{sp}}^2 + z_{\text{sp}}^2} \tag{2}$$

In equilibrium levitating state, X_0 is static displacement in x axis direction [mm], Z_0 is static displacement in z axis direction [mm] and I_0 is steady current of electromagnet [A]. The eq. (1) is linearized by performing Taylor expansion.

$$F(X_0 + \Delta x, Z_0 + \Delta z, I_0 + \Delta i) = F_0 - 2\frac{F_0 X_0}{\Gamma_0^2}\Delta x - 2\frac{F_0 Z_0}{\Gamma_0^2}\Delta z + 2\frac{F_0}{I_0}\Delta i \tag{3}$$

Where F_0 is static attractive force of equilibrium levitating state [N], Γ_0 is distance from center of electromagnet to edge of steel plate in equilibrium levitating state [mm], x is steel plate displacement in horizontal direction on equilibrium levitating state [m], z is steel plate displacement in vertical direction on equilibrium levitating state [m], i is current fluctuation value of coil [A]. In the proposed system installed so that the electromagnets are opposed to each other across the steel plate, attractive force f_1, f_2 that generated by each electromagnet suppose that occurs from the steel plate edge towards the center of each electromagnet core as shown in Fig. 9. When on the f_1 side steel plate is displaced by Δx, on the f_2 side steel plate is displaced by $-\Delta x$. Also, to perform positioning control, when on the f_1 side the current changes Δi, on the f_2 side the current changes $-\Delta i$. Also, when steel plate is displaced in z direction, both electromagnets are Δz displaced. Attractive force f_1, f_2 near the equilibrium levitating state, are as follow.

$$f_1 = F(X_0 + \Delta x, Z_0 + \Delta z, I_0 + \Delta i) \tag{4}$$

$$f_2 = F(X_0 - \Delta x, Z_0 + \Delta z, I_0 - \Delta i) \tag{5}$$

When attractive forces from both electromagnets and the angle formed by the x axis defined as θ_1, θ_2, the x direction component in attractive force ,are as follow.

$$f_1 \cos\theta_1 + f_2 \cos\theta_2$$
$$= \frac{X_0}{\Gamma_0}F(X_0 + \Delta x, Z_0 + \Delta z, I_0 + \Delta i) + \frac{X_0}{\Gamma_0}F(X_0 - \Delta x, Z_0 + \Delta z, I_0 - \Delta i)$$
$$= -4\frac{F_0 X_0^2}{\Gamma_0^3}\Delta x + 4\frac{F_0 X_0}{I_0 \Gamma_0}\Delta i \tag{6}$$

The z direction component in attractive force, are as follow.

$$f_1 \sin\theta_1 + f_2 \sin\theta_2$$
$$= \frac{Z_0}{\Gamma_0}F(X_0 + \Delta x, Z_0 + \Delta z, I_0 + \Delta i) - \frac{Z_0}{\Gamma_0}F(X_0 - \Delta x, Z_0 + \Delta z, I_0 - \Delta i)$$
$$= -4\frac{F_0 Z_0^2}{\Gamma_0^3}\Delta z + 2F_0\frac{Z_0}{\Gamma_0} \tag{7}$$

The weight of the steel plate to be supported by a pair of electromagnets is m. As, $\Delta x = -x$, $\Delta z = -z$, $\Delta i = i$ establishing the equation of motion shows it, as follows.

$$m\frac{d^2x}{dt^2}+4\frac{F_0 X_0^2}{\Gamma_0^3}x-4\frac{F_0 X_0}{I_0 \Gamma_0}i=0 \qquad (8)$$

$$m\frac{d^2z}{dt^2}+4\frac{F_0 Z_0^2}{\Gamma_0^3}z=2F_0\frac{Z_0}{\Gamma_0}-mg \qquad (9)$$

At this time, taking the values of Γ_0, Z_0, F_0 which satisfy the following equation, steel plate can be magnetically levitated.

$$2F_0\frac{Z_0}{\Gamma_0}-mg=0 \qquad (10)$$

As described above, we obtained the motion of x direction by attractive force from facing electromagnet is depend on amount of change from stationary value of pair electromagnets, the motion of z direction is depending on stationary value of electromagnet. Therefore, in this paper, focusing only on the horizontal direction, a position control model is constructed with $Z_0 = \Delta z = 0$, $\Gamma_0 = X_0$.

3.2 Horizontal positioning control model

Although the flexible thin steel plate exhibits elastic vibration in the vertical direction, it can be regarded as a rigid body in the X direction. The proposed system virtually divides the steel plate into two parts as shown in Fig. 10. We modeled the motion of the steel plate in the X direction using a 1-DOF model that actively controls each part. The same static attractive force is applied by the two installed electromagnets in order to sandwich the steel plate and, the equilibrium position of the steel plate is at the same distance from each electromagnet. The displacement of the steel plate from the equilibrium position is defined as x and the motion and circuit equations are as follows. Furthermore, the attractive force of the electromagnets at the equilibrium point was linearized.

$$m\ddot{x}=f_1-f_2=f_x \qquad (1)$$

$$f_x=\frac{4F_x}{X_0}x+\frac{4F_x}{I_x}i_x \qquad (2)$$

$$\frac{d}{dt}i_x=-\frac{L_{xeff}}{L_x}\cdot\frac{I_x}{X_0^2}\dot{x}-\frac{R_x}{2L_x}i_x+\frac{1}{2L_x}v_x \qquad (3)$$

$$L_x=\frac{L_{xeff}}{X_0}+L_{xlea} \qquad (4)$$

Using the state vector, Eqs. (1)-(4) can be rewritten as follow.

$$\dot{x}=A_x x+B_x v_x \qquad (5)$$

$$x=\begin{bmatrix} x & \dot{x} & i_x \end{bmatrix}^T$$

$$A_x=\begin{bmatrix} 0 & 1 & 0 \\ \dfrac{4F_x}{m_x X_0} & 0 & \dfrac{4F_x}{m_x I_x} \\ 0 & -\dfrac{L_{xeff}}{L_x}\cdot\dfrac{I_x}{X_0^2} & -\dfrac{R_x}{2L_x} \end{bmatrix},$$

Table 1 Coefficient of the control model.

Symbol	Value
X_0	5×10^{-3} m
L_{xeff}	1.25×10^{-5} H
L_{xlea}	1.89×10^{-1} H
L_x	1.92×10^{-1} H
R_x	$10\ \Omega$
m_x	3.74×10^{-2} kg

Table 2 Feedback gain of F_x.

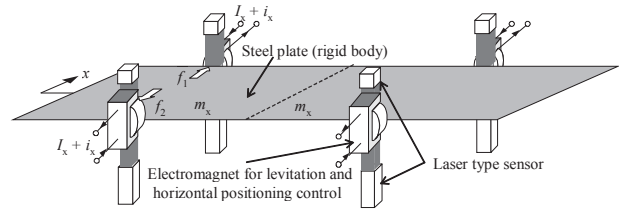| f_x	f_v	f_i
1.04×10^3	3.66×10^2	4.2×10^1

Fig. 10 Experimental model of electromagnetic

$$B_x=\begin{bmatrix} 0 & 0 & \dfrac{1}{2L_x} \end{bmatrix}^T$$

where F_x is the magnetic force of the coupled magnets in the equilibrium state [N], X_0 is the gap between the steel plate and the electromagnet in the equilibrium state [m], I_x is the current of the coupled magnets in the equilibrium state [A], i_x is the dynamic current of the coupled magnets [A], L_x is the inductance of the magnet coil in the equilibrium state [H], R_x is the resistance of the coupled magnet coils [Ω], v_x is the dynamic voltage of the coupled magnets [V], L_{xeff}/X_0 is the effective inductance of the one magnet coil [H], and L_{xlea} is the inductance leakage of the magnet. Furthermore, v_x is the feedback x, the state variable x and is expressed in the following equation.

$$v_x=-F_x x \qquad (6)$$

$$F_x=\begin{bmatrix} f_x & f_v & f_i \end{bmatrix}$$

4. Levitation Experiment of Steel Plate by Edge Supported Electromagnetic Levitation System

4.1 Experimental conditions

The steady current I_x of the electromagnet was varied. In order to evaluate the levitating characteristics of the steel plate at that time, we carried out a magnetic steel plate experiment. The steel plate is supported by jack, and levitated by lowering the jack. The parameter that was used to design the control system is shown Table 1.
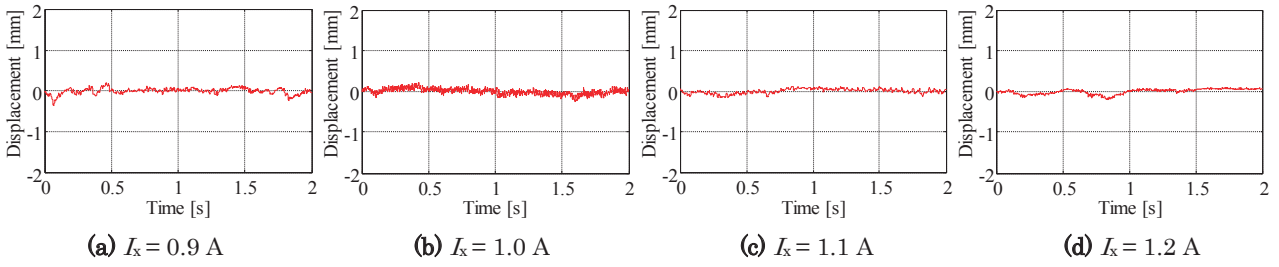
(a) I_x = 0.9 A   (b) I_x = 1.0 A   (c) I_x = 1.1 A   (d) I_x = 1.2 A

Fig. 11   Time histories of the horizontal displacement x of the steel plate.

(a) I_x = 0.9 A   (b) I_x = 1.0 A   (c) I_x = 1.1 A   (d) I_x = 1.2 A
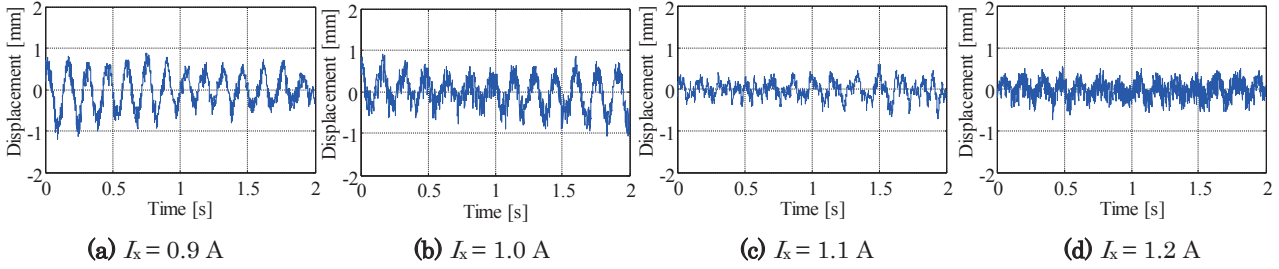
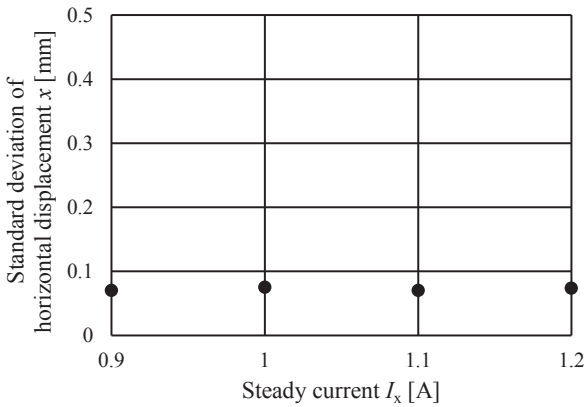**Fig. 12**   Time histories of the vertical displacement z of the steel plate.

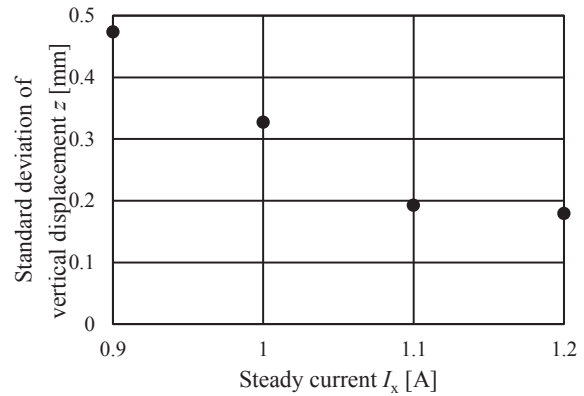**Fig. 13**   Relationship between the steady current I_x and the standard deviation of the horizontal displacement x.

Fig. 14   Relationship between the steady current I_x and the standard deviation of the vertical displacement z.

Furthermore, we searched for the feedback gain F_x of equation (6), which was determined by trial and error and is shown in Table 2. For the experimental conditions, the range of steady current was changed to $I_x = 0.9 \sim 1.2$ A.

At each steady current, there is a position where the steel plate could levitate. We searched the position where the steel plate could levitate at each steady current value by trial and error. The standard deviation of displacement was calculated in order to evaluate the displacement amplitude in the x and z directions of the steel plate. The experiment was conducted five times for each condition and for the evaluation the average of the results was used.

4.2 Experimental results

Figure 11 shows the time history of the displacement of the steel plate in the x direction. Figure 12 shows the time history of the displacement of the steel plate in the

z direction. Figure 11 and Fig. 12 both show the results of each steady current of (a) 0.9 A, (b) 1.0 A, (c) 1.1 A, and (d) 1.2 A. Figure 13 summarizes the relationship between the steady current and the standard deviation of the x direction in each steady current. The standard deviation of displacement in the x direction was suppressed to 0.1 mm or less in all steady currents. Even in the proposed magnetic levitation system, the sufficiently positioned control in the x direction. Figure 14 summarizes the relationship between the steady current and the standard deviation of the z direction in each steady current. Comparing the results in Fig. 14 for each steady current value, by increasing the steady current value a suppression in vibration of the z direction was confirmed. In the case of the minimum steady current, $I_x = 0.9$ A, the standard deviation of the z direction is 0.474 mm. In the case of the maximum steady current, $I_x = 1.2$ A, the standard deviation of the z direction is 0.179 mm. When the steady currents 0.9A and 1.2A were compared, the vibration in the z direction could be suppressed by 62%.
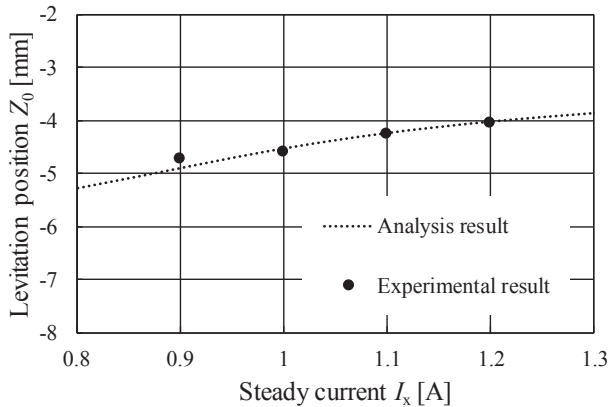
Fig. 15 Relationship between steady current I_x and levitation position Z_0.

As the steady current I_x of the electromagnet increased, the tension applied to the steel plate in the x direction increased. As a result, it is considered that the restoring force in the z direction increased and the vibration of the steel plate in the z direction could be suppressed.

5. Levitation Position Measurement Experiment of Steel Plate of Vertical Displacement

For the experimental conditions similar to chapter 4, the range of steady current was changed to $I_x = 0.9 \sim 1.2$ A. The levitation position in the z direction was measured five times for each condition. The average of those results is the experimental value. Figure 15 shows the levitated position of the steel plate in each measured steady current. The dashed line in Fig. 15 which is extracted from the analysis results in Fig. 7 shows the relationship between the levitation position Z_0 and the steady current I_x at which the steel plate levitates. Plots in Fig.15 are averaged experimental results. As a result, when the steady current is the minimum, $I_x = 0.9$ A, the levitation position of the vertical direction was 0.474 mm. In contrast when the steady current is the maximum, $I_x = 1.2$ A, the levitation position of the vertical direction was 0.402 mm. The levitated position of the steel plate increase by 0.7 mm. Furthermore, the trend of the experimental values agreed with the analysis result. We confirmed the effectiveness of the electromagnetic field analysis. As a result, using electromagnetic field analysis, even for steel plates of different thickness and material, we confirmed that we could establish such a system's design guidelines.

6. Conclusion

In this study, we constructed a prototype of an edge supported type magnetic levitation system applying electromagnetic force only from the X direction of a steel plate. We verified the levitating characteristics of the proposed control system. We carried out levitation experiments using an ultra-thin steel plate of 0.24 mm. We confirmed the achieved stable levitation. Furthermore, we carried out levitation experiments by changing the steady current value of the electromagnet. The experimental and analytic results of the calculated vertical levitating position agree with each other. The results showed that it is, possible to experimentally construct a control system for the steel plate stationary vertical direction displacement. In this study, we confirmed the effectiveness of the proposed magnetic levitation system. However, under transient conditions there were instance when it became practically an unstable system. In order to solve the problem, it is necessary to construct a control system that changes steady-state current by feedback of vertical displacement in addition to the proposed control system in this paper. For the future, we will consider in detail a more effective sensing method and modeling for the stability of this method. Furthermore, the shape of the electromagnet to generate more effective attractive force to flexible steel plate would be considered.

References

1) O. Suzuki, T. Nakagawa: *J. Jpn. Soc. App. Elec. Mech.*, **25**, 118 (2017), [in Japanese].
2) K. Matsushima, F. Kato, T. Ohji, K. Amei, M. Sakui: *J. Jpn. Soc. App. Elec. Mech.*, **21**, 296 (2013), [in Japanese].
3) M. Morishita, M. Akashi: *Workshop of The Institute of Electrical Engineers of Japan*, LD-98-36, (1998), [in Japanese].
4) K. Sato, S. Torii: *Trans. IEEJ*, **128**, 267 (2008), [in Japanese].
5) T. Mizuno, D. Sekine, M. Takasaki, Y. Ishino: *Trans. Jpn. Soc. Mech. Eng.*, **80**, DR0163 (2014), [in Japanese].
6) T. Narita, T. Kurihara, H. Kato, Y. Oshinoya: *Mech. Eng. Jour.*, **3,** 15-00376 (2016).
7) T. Kurihara, T. Narita, H. Kato: *Int. J. App. Elec. Mech.*, **52**, 1495(2016).
8) T. Narita, M. Kida, T. Suzuki, H. Kato: *J. Magn. Soc. Jpn.*, **41,** 14(2017).

Notice for Photocopying

If you wish to photocopy any work of this publication, you have to get permission from the following organization to which licensing of copyright clearance is delegated by the copyright owner.

⟨All users except those in USA⟩
Japan Academic Association for Copyright Clearance, Inc.（JAACC）
6–41 Akasaka 9-chome, Minato-ku, Tokyo 107–0052 Japan
Phone 81–3–3475–5618　FAX 81–3–3475–5619　E-mail: info@jaacc.jp

⟨Users in USA⟩
Copyright Clearance Center, Inc.
222 Rosewood Drive, Danvers, MA01923 USA
Phone 1–978–750–8400　FAX 1–978–646–8600

複写をされる方へ

本会は下記協会に複写に関する権利委託をしていますので，本誌に掲載された著作物を複写したい方は，同協会より許諾を受けて複写して下さい．但し（社）日本複写権センター（同協会より権利を再委託）と包括複写許諾契約を締結されている企業の社員による社内利用目的の複写はその必要はありません．（社外頒布用の複写は許諾が必要です．）
権利委託先：一般社団法人学術著作権協会
　　　　　〒107–0052 東京都港区赤坂9–6–41　乃木坂ビル
　　　　電話（03）3475–5618　FAX（03）3475–5619　E-mail: info@jaacc.jp
なお，著作者の転載・翻訳のような，複写以外の許諾は，学術著作権協会では扱っていませんので，直接本会へご連絡ください．